Effects of Body-Side Compression on Forward-Swept Sidewall Compression Inlets

Patrick E. Rodi*

NASA Langley Research Center, Hampton, Virginia 23681-0001

Forward-swept sidewall compression inlets have been tested at Mach 4 to study the effects of body-side compression surfaces on inlet performance. The measurements include mass flow capture and mean surface pressure distributions obtained during simulated combustion-induced pressure increases downstream of the inlet. Inlet performance is evaluated using starting and unstarting characteristics, mass capture, mean surface pressure distributions, and permissible back-pressure limits. The results indicate that inlet performance can be improved with selected body-side compression surfaces placed between the inlet sidewalls.

Nomenclature

AR = aspect ratio of isolator, height/spanwise width
C_w = cowl position in percent of T_x, $100(C_x/T_x)$
C_x = streamwise distance ahead of isolator
CR_a = aerodynamic contraction ratio, $CR_g\dot{m}$
CR_g = geometric contraction ratio
g = spanwise distance between sidewalls within isolator
H = inlet height, 1.87 in., 4.75 cm
$\dot{m}$ = normalized inlet mass capture
P_b = maximum back pressure
P_c = maximum cowl pressure
P_{th} = throat pressure
P_1 = freestream static pressure
T_x = streamwise distance from sidewall leading edge to leading edge of isolator, 5.08 in., 12.9 cm
W = inlet spanwise width at sidewall leading edge
X = streamwise distance measured downstream from the baseplate leading edge
X_c = streamwise location of vortex–vortex interaction
Y = spanwise distance measured from the inlet centerline
Z = vertical distance from the baseplate surface
δ_∞ = incoming boundary-layer thickness

Introduction

HIGH Mach number air-breathing propulsion systems generally focus on vehicle-integrated supersonic combustion ramjets (scramjets) (Fig. 1). Such systems require careful design of primary engine components to effectively exploit the potential of propulsion–airframe integration. The engine inlet is one such component. The three-dimensional sidewall compression inlet concept has been under study for many years. Investigations of overall performance characteristics have been made using a variety of geometries over a range of conditions.[1-6]

One problem facing the engine designer is providing for low Mach number starting capability. This requirement is generally in conflict with the high contraction ratio and high mass capture required for thrust at higher Mach numbers. Variable geometry may solve this problem, but the accompanying weight and complexity might be avoided by careful

design of the compression surfaces. Sidewall compression inlets with leading edges swept aft (i.e., swept downstream) can deflect significant amounts of mass at low Mach numbers to permit starting while still obtaining high mass capture at high Mach numbers. Forward-swept compression inlets (i.e., upstream swept leading edges) can have greater mass capture and reduced cowl shock wave strengths, as compared to inlets sidewalls with no sweep or aft sweep. However, these inlets are generally more difficult to start at the low Mach numbers.

The dominant feature found in the sidewall compression inlet flowfield is a pair of glancing shock-wave/boundary-layer interactions caused by the sidewall-induced shock waves sweeping across the incoming boundary layer. The most simple interaction of this type is that generated by a single compression surface. Much has been learned of these interactions and the reader is directed towards the reviews by Settles and Dolling.[7,8] One important result is that the incoming boundary layer separates, for all but the very weakest interactions, and rolls up into a strong vortex located near the root of the compression surface. A number of studies have been conducted to examine the crossing shock–shock-wave interaction formed by two compression surfaces.[9-11] These investigations detail a complex flowfield with numerous shock waves and a strong vortex–vortex interaction occurring along the flowfield centerline adjacent to the body surface. In this vortex–vortex interaction, the vortices lift off of the surface and create a large core of low total pressure fluid near the middle of the cross-plane. A sketch of one such flowfield made by Garrison et al.,[10] based upon planar laser scattering images, is shown in Fig. 2. Similar flowfield structures have been seen numerically.[5,9]
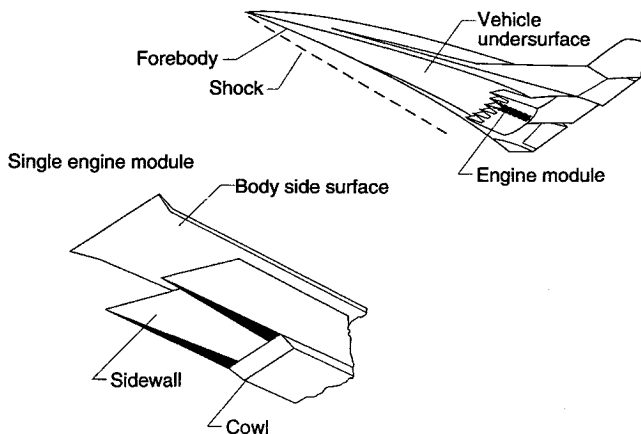
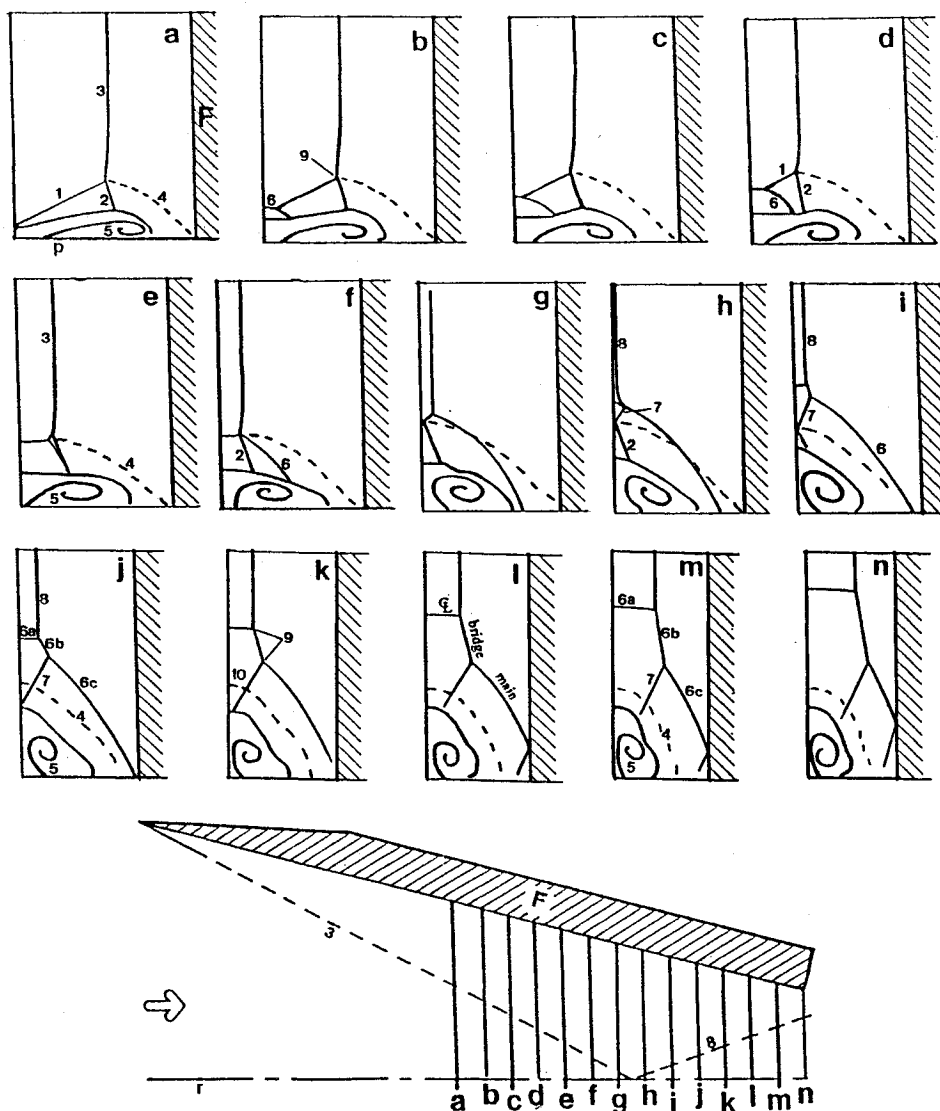Fig. 1 Airframe integrated propulsion system.

Fig. 2 Crossing-shock interaction flowfield from Ref. 10.

With an increased understanding of the flowfield, designers have worked to improve inlet performance. In a recent study at Mach 4, a compression surface (i.e., ramp) located between forward-swept sidewalls was used to deflect mass, thereby improving the low Mach number starting characteristics.[12] Although the results were encouraging, only one compression surface geometry was tested.

In the current investigation, the effects of body-side compression surfaces are more fully examined by testing a number of compression ramp geometries on forward-swept sidewall compression inlets at Mach 4. The following are the objectives:

1) Examine the starting characteristics of these inlets when ingesting a turbulent boundary layer.

2) Measure the mean surface pressure distributions and determine the maximum permissible back pressure before unstart.

3) Measure the inlet mass capture.

4) Evaluate the performance changes induced by the ramps.

Experimental Program

The experiments were performed in the 9 × 9 in. (22.9 × 22.9 cm) NASA Langley Mach 4 Blowdown Facility. The tunnel was operated using unheated air at a freestream Mach number of 4.03, total pressure of 200 ± 2 psia (1.38 MPa ± 34.5 kPa), and total temperature of 510 ± 3°R (283 ± 2 K),

resulting in a freestream Reynolds number of 21.0 × 10⁶/ft (65.6 × 10⁶/m). Although the total temperature did not significantly vary during a given run, the temperature could change from run-to-run by as much as ±15°R. The model was initially at ambient temperature (525°R, 292 K). These conditions produced a moderately warm wall condition with an actual wall temperature-to-adiabatic wall temperature ratio of 1.11.

The inlet model, shown schematically in Fig. 3, was made of aluminum and was 12.81 in. (32.5 cm) long and 1.87 in. (4.75 cm) high. The sidewalls had a 6-deg turning angle with the leading edges swept forward at 30 deg. The shoulders at the upstream end of the constant area section (i.e., isolator) were also swept forward at 30 deg. The sidewall corners at the rear of the constant area section were unswept creating an isolator 1.50 in. (3.81 cm) in length on the bodyside of the model and 2.58 in. (6.55 cm) in length on the cowl side. The inlet sidewalls were mounted to an aluminum baseplate. A 12-in.- (30.5-cm-) long flat plate was mounted ahead of the baseplate upon which the incoming turbulent boundary layer was developed. The sidewall leading edges were located 13.84 in. (35.2 cm) downstream of the leading edge of the boundary-layer plate. This streamwise location permitted natural transition of the boundary layer to occur well upstream of the inlet. A two-dimensional boundary-layer code[13] was used to calculate the properties of the incoming turbulent boundary
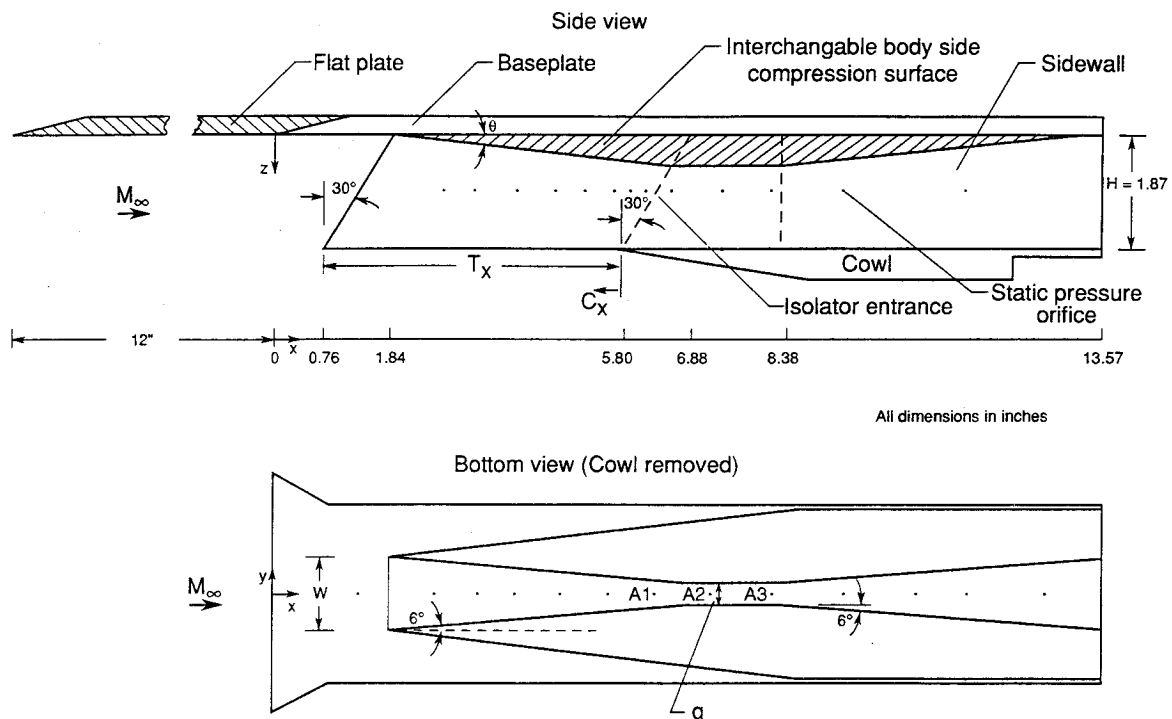
Fig. 3 Forward-swept sidewall compression inlet model.

Table 1 Experimental test configurations

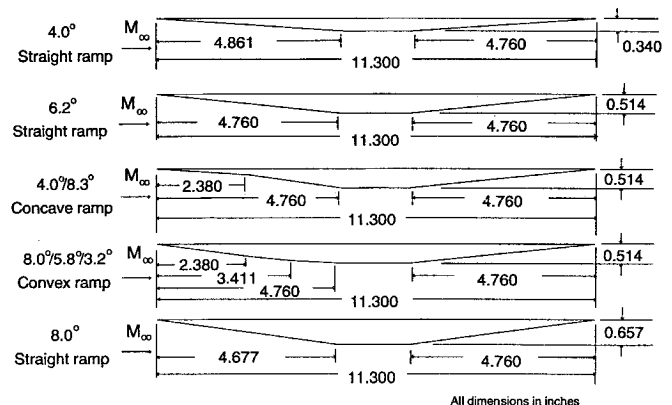| W/g	Ramp, deg	CR_g	AR
3.0	0 (no ramp)	3.0	3.53
3.0	4.0	3.67	2.89
3.0	6.2	4.14	2.56
3.0	4.0/8.3	4.14	2.56
3.0	8.0/5.8/3.2	4.14	2.56
3.0	8.0	4.62	2.29
4.0	0 (no ramp)	4.0	5.34
4.0	4.0	4.92	4.38
4.0	6.2	5.56	3.87
4.0	4.0/8.3	5.56	3.87
4.0	8.0/5.8/3.2	5.56	3.87
4.0	8.0	6.21	3.47

Fig. 4 Body-side compression surfaces.

layer and the results at the streamwise location of the sidewall leading edges are listed:

Boundary-layer thickness, δ	0.195 in.
Displacement thickness, δ^*	0.082 in.
Momentum deficit thickness, θ	0.010 in.
Reynolds number based upon θ, Re_θ	1.6256×10^4
Skin friction coefficient, C_f	0.00112
Boundary-layer thickness/inlet height, δ/H	0.1

This solution is in agreement with earlier experimental measurements.[14]

Measurements include surface flow visualization, mean surface pressure, and mass capture. The kerosene–lampblack surface tracer technique[15] was used to obtain surface flow visualization on four of the configurations. The mean surface pressure was measured at a number of model locations, as shown in Fig. 3. These measurements were obtained using conventional pressure taps connected to four electronically scanned pressure (esp) modules. The model pressure data were measured by a separate data acquisition/buffer system and then transferred to a personal computer. The personal computer was also used to measure four additional channels for tunnel conditions and flow-meter position through a separate A/D board. All data channels were sampled at 1 Hz.

A flow meter was attached to the rear of the model. The flow meter was used to measure inlet mass capture and could be used to simulate the increased pressure downstream of the inlet due to combustion by reducing the exit area.

Five body-side compression surfaces (i.e., ramps) were tested at inlet width-to-gap ratios W/g, of 3.0 and 4.0. These ramp geometries are listed in Table 1 and are shown in Fig. 4. The local ramp angles are measured from the freestream direction. The ramps were positioned with their leading edges at the same streamwise position as the sidewall leading edges. The combined sidewall and body-side compression produced geometric contraction ratios CR_g from 3.0 to 6.21. AR of each isolator cross section (height/spanwise width) is also listed in Table 1.

The 8.0-/5.8-/3.2-deg convex ramp and the 4.0-/8.3-deg concave ramp were designed to match the geometric contraction ratio of the 6.2-deg straight ramp. The major difference between these configurations is the pressure field ahead of the isolator induced by the ramps. The 8.0-/5.8-/3.2-deg convex ramp was designed to reduce the adverse pressure gradient ahead of the isolator and modify the vortex–vortex interaction. It was hoped that by modifying the local pressure field, the vortex lifting phenomena could be delayed or eliminated

Table 2 Inlet starting behavior and mass capture

W/g	Ramp, deg	CR_g	C_w, %	Starting behavior	$\dot{m}$, %	CR_a
3.0	0 (no ramp)	3.0	0	PS,[a] U,[b] SS[c]	79	2.38
3.0	4.0	3.67	0	PS, U, SS	79	2.89
3.0	6.2	4.14	−2	PS, U, SS	77	3.20
3.0	4.0/8.3	4.14	−2	DNS[d]	N/A[e]	N/A
3.0	8.0/5.8/3.2	4.14	0	PS, U, SS	79	3.29
3.0	8.0	4.62	−2	PS, U, SS	78	3.60
4.0	0 (no ramp)	4.0	−16	DNS	N/A	N/A
4.0	4.0	4.92	−16	DNS	N/A	N/A
4.0	6.2	5.56	−16	PS, U, SS	68	3.80
4.0	4.0/8.3	5.56	−21	DNS	N/A	N/A
4.0	8.0/5.8/3.2	5.56	−8	PS, U, SS	73	4.08
4.0	8.0	6.21	−16	DNS	N/A	N/A

[a]The inlet pulse-started.
[b]The inlet unstarted by increased back pressure.
[c]The inlet successfully self-started.
[d]The inlet did not pulse-start.
[e]Not applicable or not available.

and superior inlet performance obtained. The 4.0-/8.3-deg concave ramp was designed to increase the pressure gradient as a further test of this effect.

Results and Discussion

Starting Behavior

For maximum thrust, an inlet must process a large amount of mass as efficiently as possible. Also, an engine should be self-starting in the event that a perturbation (e.g., combustion unsteadiness) causes an unstart. Consequently, starting behavior is important in the evaluation and selection of engine inlet geometries. In blowdown tunnel experiments where the model is exposed to the airflow during the startup process (such as in this study), two types of inlet starts are possible. The first is called a "pulse-start." In this scenario, the rapid startup of the tunnel assists the inlet to start. The second type is called a "self-start." If an operating inlet has been forced to unstart and then restarts without modifying the geometry or test conditions, the inlet is defined as being self-starting at those test conditions. Self-starting is the desirable engine characteristic.

On this model, the cowl could be located over a range of positions at and downstream of the leading edge of the isolator. Within this range, a number of inlets operated successfully. The inlet starting behaviors are summarized in Table 2. In this table results are shown at the most upstream cowl position for configurations that operated (i.e., operating at the greatest mass capture). Results are shown at the most downstream cowl position for configurations that would not pulse-start or self-start (i.e., at the most conducive cowl position for starting). Although not generally true, in this study every configuration that pulse-started also self-started.

At $W/g = 3.0$, only the 4.0-/8.3-deg concave ramp did not start. This is despite the fact that the 8.0-/5.8-/3.2-deg convex ramp and the 4.0-/8.3-deg concave ramp were designed with the same geometric contraction ratio of the 6.2-deg straight ramp. This indicates the ramp geometry can play an important role in permitting inlet starting. The 8.0-/5.8-/3.2-deg convex ramp operated with the cowl at a further upstream position than was possible with the 6.2-deg straight ramp.

For $W/g = 4.0$, many of the inlet configurations did not start. The 6.2-deg straight ramp was the only straight-ramp configuration to start. This result indicates that the angle selected for even simple, straight-ramp geometries is critical to achieve the proper mass dumping and total pressure recovery combination for operation. The 8.0-/5.8-/3.2-deg convex ramp configuration successfully pulse-started and self-started and operated with the cowl positioned further upstream than with the 6.2-deg straight ramp. The inlet did not pulse-start when using the concave ramp, even with the cowl placed as far

downstream as $C_w = −21\%$. This reaffirms the result at $W/g = 3.0$, the shape of the body-side compression ramp is an important factor in permitting inlet operation and clearly indicates that the concave shape is not conducive to inlet starting.

Mass Capture

The inlet mass capture is important for determining thrust for a given engine. The sixth column in Table 2 lists the normalized mass capture $\dot{m}$ for each configuration. This value is expressed as a percentage of the mass transport across the inlet frontal area at freestream conditions $(\rho_\infty U_\infty WH)$, where ρ_∞ and U_∞ are the freestream density and velocity, respectively. The captured mass flow was calculated from measurements of the wall pressure just ahead of the throat of the flow meter and the flow meter exit area. A Kline and McClintock[16] error analysis indicates that the calculated mass flow values have an uncertainty of $\pm7\%$. The last column in Table 2 lists the aerodynamic contraction ratio CR_a, which is defined here as the product of the normalized mass capture and the geometric contraction ratio.

At $W/g = 3.0$, each inlet captured approximately the same amount of mass. The 8.0-/5.8-/3.2-deg convex ramp configuration permitted operation with the cowl positioned further upstream than with the 6.2-deg straight ramp. At $W/g = 4.0$, the 8.0-/5.8-/3.2-deg convex ramp again permitted operation with the cowl further forward than was possible with the 6.2-deg straight ramp. Moving the cowl forward should have the effect of increasing the inlet mass capture. The data showed an increase in mass capture of 7%. However, this value is also the uncertainty of the measurement. The 8.0-/5.8-/3.2-deg convex ramp at $W/g = 4.0$ demonstrated the highest $CR_a = 4.08$ of all the geometries tested in this study.

Kerosene–Lampblack Patterns

The kerosene–lampblack carrier fluid/pigment flow visualization technique[15] has been used to determine the local shear stress direction for four selected inlet configurations. This technique has been used by a number of researchers studying similar crossing-shock-induced interactions,[10,11] and is particularly suited for use in a blowdown facility. The fine details of the resulting patterns do not reproduce well. Therefore, sketches of the patterns are used in the following discussion.

Sketches of the sidewall streak patterns for the four selected configurations are shown in Fig. 5. For cases with a ramp, the influence of the ramp's shock wave on the sidewall boundary layer is clearly seen as a diagonal line of material accumulation, originating from the ramp leading edge. This ramp-induced shock wave appears to separate the sidewall
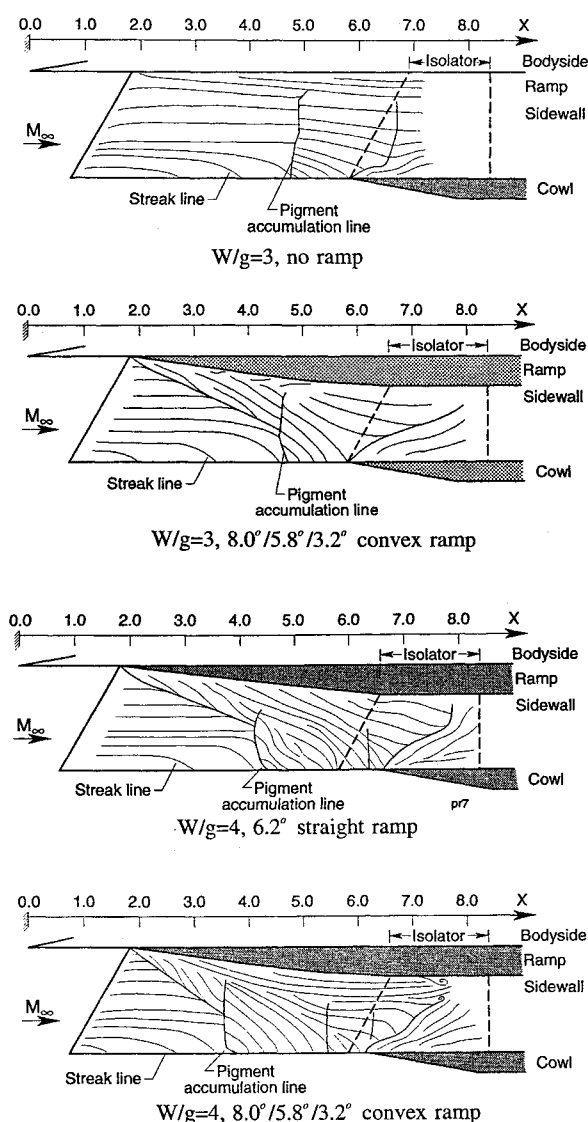
W/g=3, no ramp

W/g=3, 8.0°/5.8°/3.2° convex ramp

W/g=4, 6.2° straight ramp

W/g=4, 8.0°/5.8°/3.2° convex ramp

Fig. 5   Sketch of the kerosene–lampblack flow visualization patterns on the inlet sidewalls.
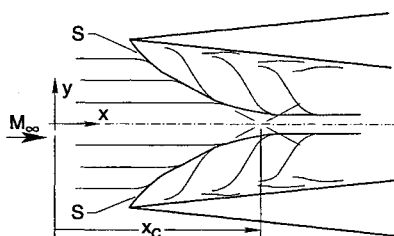

Fig. 6   Sketch of the kerosene–lampblack patterns on the baseplate.

boundary-layer flow for the 6.2-deg straight ramp and the 8.0-/5.8-/3.2-deg convex ramp geometries. The vertically orientated pigment accumulations, such as at $X = 4.7$ in. (11.9 cm) and $X = 6.9$ in. (17.5 cm) for the $W/g = 3.0$, no-ramp case, are created by a locally strong adverse pressure gradient generated by the impingement of the crossing oblique shock waves. Note that the initial swept-forward orientation of the sidewall shock waves is largely absent at the first impingement location. This unswept orientation is maintained throughout the remainder of the inlet flowfield. A similar behavior was seen in every other pattern and has been observed numerically with similar configurations incorporating forward-swept leading edges.[5] The streak patterns also show a large amount of

turning present along the sidewall. This turning is especially severe just ahead of the cowl leading edge. The influence from the swept-shock interaction generated by the cowl shock and sidewall boundary layer is clearly seen on the walls of the isolator.

Streak patterns were also made along the ramp surface. The four patterns are very similar to each other. A representative sketch of these patterns is shown in Fig. 6. In crossing-shock-wave-dominated flowfields, such as in these inlets, the swept-shock wave usually separates the incoming boundary, which then rolls into a strong vortex just above the surface (as shown in Fig. 2). The body-side surface flow pattern is a result of these two swept-shock interactions and their mutual interactions along the flowfield centerline. Every pattern clearly showed the separation line (marked with an "S") formed by each swept-shock interaction. These lines, which are very curved near the sidewall/body-surface intersection, become straight a short distance from the sidewalls. As the separation lines approach one another, they curve parallel to each other near the flowfield centerline. As a measure of the location where the two vortices interact, the straight portions of the separation lines can be extended until they meet on the flowfield centerline. The streamwise distance to this point X_c varied between 3.14 in. (8.0 cm) for the $W/g = 3.0$, no-ramp case to 3.39 in. (8.6 cm) for the $W/g = 3.0$, 8.0-/5.8-/3.2-deg case.

Surface Pressure Distributions

The mean static wall pressure was measured at various locations along the ramp surface, inlet sidewall, and cowl. The pressure distributions on the ramp surface along the centerline of the inlet, normalized by the freestream pressure P_1 are shown in Fig. 7. (A sketch of the inlet is provided to aid the reader. A representative ramp and cowl have been added in dashed lines. The vertical arrows indicate the streamwise locations of the pressure taps.) As the ramp angle is increased, the pressure levels are progressively higher from the inlet leading edge to the isolator. In each figure, the effect of the convex ramp in altering the pressure distribution can be seen in the region ahead of the isolator, $X < 7.0$ in. (17.8 cm). The pressure distributions generated by the convex ramps are similar to those of the 8.0-deg straight ramps for $X < 4.0$ in. (10.2 cm), as expected. The expansion corners of the convex ramps are located at $X = 4.25$ in. (10.8 cm) and $X = 5.28$ in. (13.4 cm). The reduced pressure downstream of each expansion is clearly visible.

Figure 8 shows the pressure distribution along the sidewall centerline. (The filled circles on the sketch represent the lo-
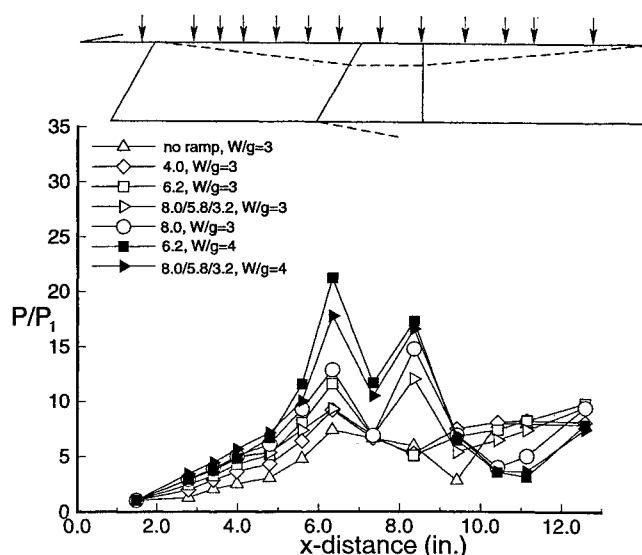

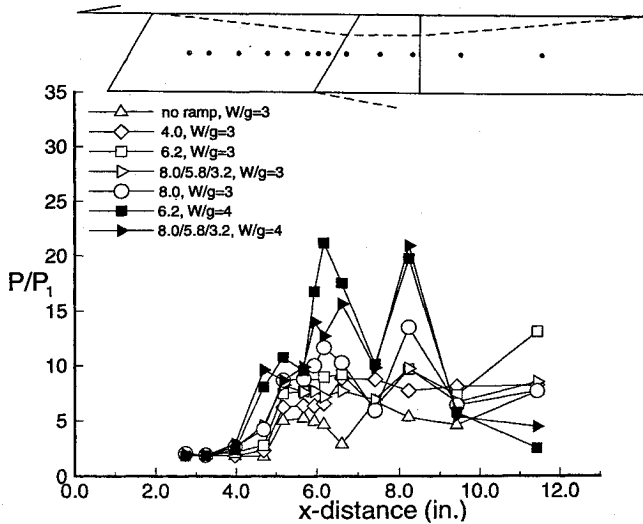Fig. 7   Body-side centerline surface pressure distributions.

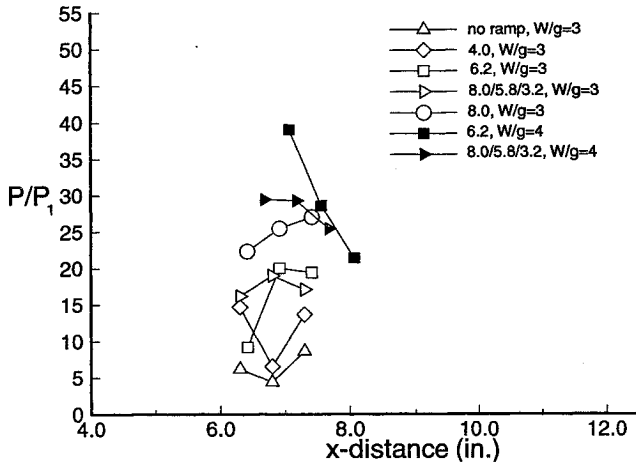Fig. 8 Sidewall centerline pressure distributions.

Fig. 10 Typical body-side centerline pressure distribution during increasing back pressure.

Fig. 9 Cowl centerline pressure distributions.

Fig. 11 Body-side centerline pressure distributions at maximum back pressure.

cations of the pressure taps.) As was seen along the body-side centerline, the pressure distribution generated by the 8.0-/5.8-/3.2-deg convex ramp is similar to that for the 8.0-deg straight ramp until downstream of the expansion corners.

Pressure measurements were also made on the inside cowl surface. Three pressure taps were located along the cowl centerline 0.50, 1.00, and 1.50 in. (1.27, 2.54, and 3.81 cm) downstream of the cowl leading edge. The normalized cowl centerline pressure distributions are shown in Fig. 9. The cowl pressures increase with increasing ramp angle, as expected, due to the additional flow turning that strengthens the cowl shock and, consequently, the cowl pressure. From an airframe perspective, a low cowl pressure is desirable to ease the structural loading on the engine.

Back-Pressure Performance

The maximum permissible back pressure that an inlet can sustain before unstart is related to the amount of thrust that can be produced. For greatest performance, the permissible back pressure should be as high as possible. Figure 10 illustrates typical inlet behavior as the back pressure is increased. The effect of increased back pressure (through decreased flow meter exit area, curves no. 1–4) can be seen. Just before unstart, the inlet reaches the maximum permissible back pressure (curve no. 4). Any further increase in back pressure causes the inlet to unstart (curve no. 5). The pressure increase observed ahead of the cowl for the unstarted condition is a result of the detached shock system characteristic of nonop-
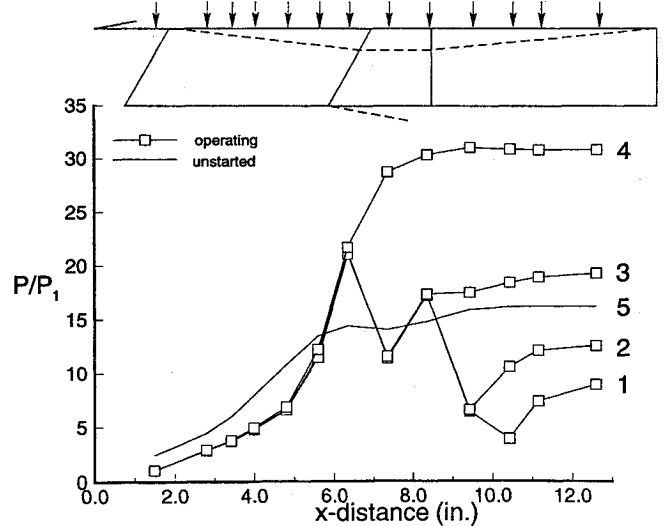

Fig. 12 Sidewall centerline pressure distributions at maximum back pressure.

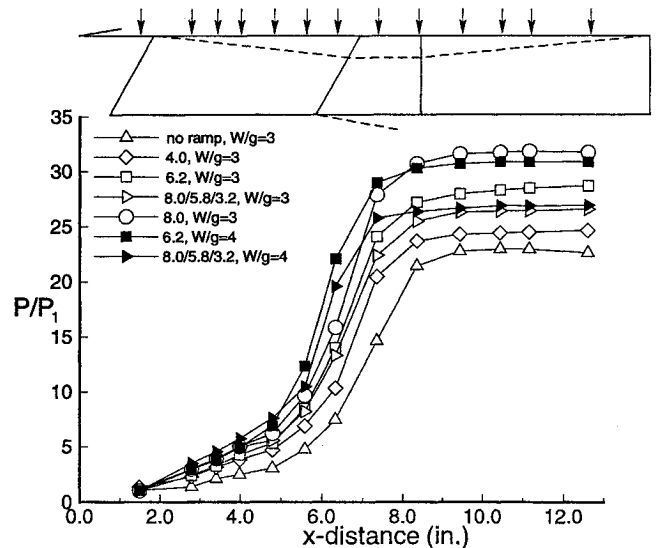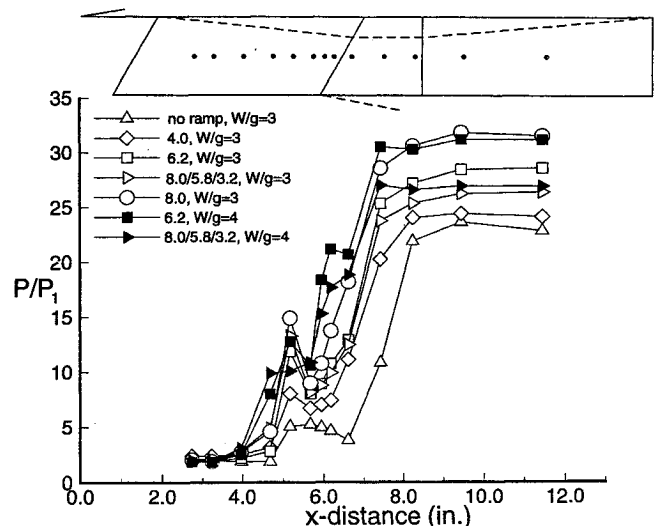Table 3 Inlet back-pressure performance

W/g	Ramp, deg	CR_g	P_b/P_1	P_c/P_1	P_{th}/P_1	$(P_b - P_{th})/P_1$
3.0	0 (no ramp)	3.0	21.4	8.9	7.4	14.0
3.0	4.0	3.67	23.7	20.0	9.2	14.5
3.0	6.2	4.14	27.2	16.5	11.6	15.6
3.0	8.0/5.8/3.2	4.14	26.6	20.1	9.3	17.3
3.0	8.0	4.62	30.3	30.9	12.9	17.4
4.0	6.2	5.56	30.3	53.7	21.2	9.1
4.0	8.0/5.8/3.2	5.56	27.3	37.4	17.8	9.5

Fig. 13 Cowl centerline pressure distributions at maximum back pressure.
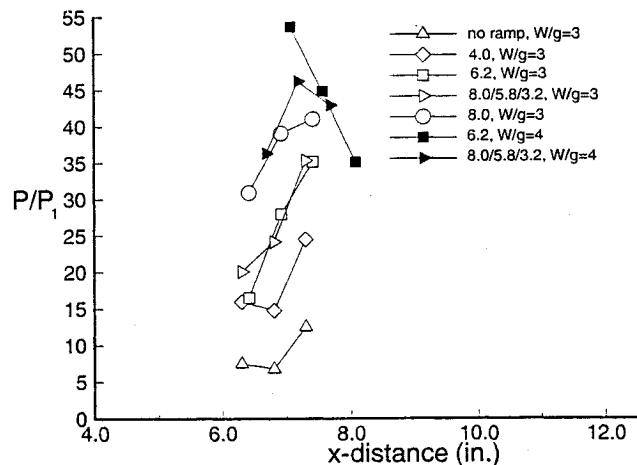
Fig. 14 Normalized back pressure–throat pressure vs normalized throat pressure.

erating inlets. This system permits much of the air to spill around the inlet, substantially reducing the captured mass flow. Figures 11 and 12 show the body-side centerline and sidewall centerline pressure distributions at maximum back pressure, respectively. The large pressure rise occurring within each inlet is clearly seen. The highest downstream pressure at which the inlet would remain operating is defined as the maximum back pressure P_b (measured at tap A3 in Fig. 3). A summary of the back-pressure performance is presented in Table 3.

At W/g = 3.0, the maximum permissible back pressure increased with ramp angle. The 8.0-/5.8-/3.2-deg convex ramp did not demonstrate as high a permissible back pressure as the 6.2-deg straight ramp. At W/g = 4.0, a similar result is seen. The W/g = 3.0, 8.0-deg straight ramp and the W/g = 4.0, 6.2-deg straight-ramp geometries demonstrated the highest permissible back pressures of the geometries studied of just over $30P_1$.

The normalized cowl centerline pressure distributions at maximum back pressure are shown in Fig. 13. The most upstream tap of the centerline row is used to define the cowl pressure P_c. The maximum normalized cowl pressure is listed in Table 3. While the 6.2-deg straight ramp and the 8.0-/5.8-/3.2-deg convex ramp demonstrated similar cowl pressure distributions at W/g = 3.0, the convex ramp geometry displayed significantly lower cowl pressure than the 6.2-deg straight ramp at W/g = 4.0.

The mass capture, maximum back pressure, and cowl pressure results for the W/g = 4.0, 6.2-deg straight ramp of the current study are significantly higher than those reported in Ref. 12. These differences are probably due to air leakage from the model in the earlier work. Initially, the same experimental setup was used as that in Ref. 12. Concern over the possibility of model leakage led to the resealing of the inlet model. When the results with the resealed model were observed to differ significantly from those seen before resealing, the model and flow meter were completely rebuilt to prevent leakage. This has been confirmed by the kerosene–
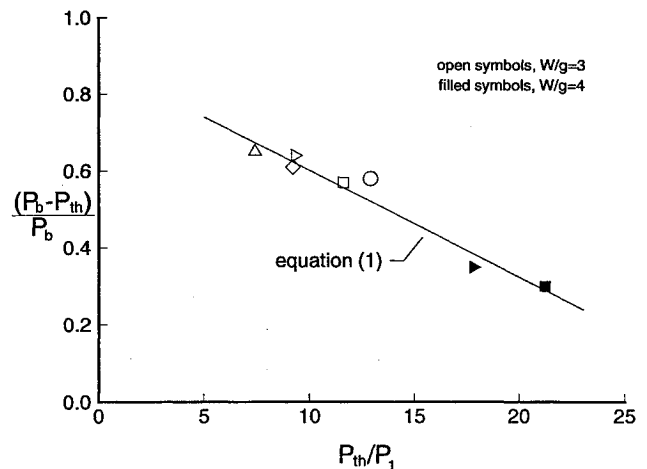
lampblack tracer technique that did not show any evidence of model leakage.

A measure of the pressure rise from the inlet-induced compression is represented by the throat pressure P_{th}, defined as tap A1 in Fig. 3 (X = 6.34 in., 16.1 cm). The throat pressure is the highest pressure measured within the inlet before back pressure is applied. The normalized throat pressure P_{th}/P_1 is listed in Table 3 for each configuration. The difference between the maximum permissible back pressure and the throat pressure represents the amount of combustion-induced pressure increase that can be tolerated. This difference, normalized by the freestream static pressure, is also listed in the table. At W/g = 3.0, the difference between maximum back pressure and throat pressure increased with ramp angle. At W/g = 3.0, the 8.0-/5.8-/3.2-deg convex ramp and the 8.0-deg straight ramp demonstrated the greatest difference between maximum back pressure and throat pressure. However, this difference was obtained with lower throat and cowl pressures for the convex ramp. At W/g = 4.0, again the 8.0-/5.8-/3.2-deg convex ramp demonstrated a superior level of pressure difference with throat and cowl pressures significantly lower than with the 6.2-deg straight ramp. Therefore, the convex ramps appear to reduce cowl pressure loading while actually increasing back-pressure performance.

The difference between the maximum back pressure and the throat pressure, normalized by the maximum back pressure $(P_b - P_{th})/P_b$, is plotted against the normalized throat pressure in Fig. 14. When this term is zero, no combustion-induced pressure increase can occur before inlet unstart. When this term is unity, the throat pressure is negligible and all of the permissible back pressure is due to the combustion-induced pressure increase. As can be seen in the figure, the current results show a general trend of a decreasing proportion of combustion-induced pressure with increasing normalized throat pressure. The solid line represents the least-squares linear fit:

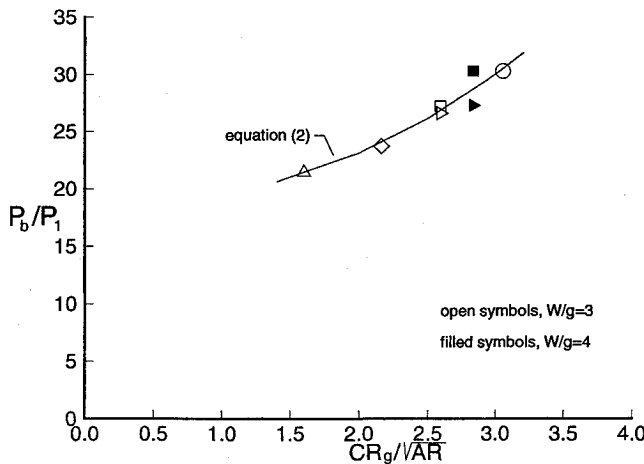$$(P_b - P_{th})/P_b = -0.028(P_{th}/P_1) + 0.883 \qquad (1)$$

Fig. 15 Inlet back-pressure performance correlation.

At both $W/g = 3.0$ and 4.0, comparisons between the 6.2-deg straight ramp and the 8.0-/5.8-/3.2-deg convex ramp indicate that the convex ramp geometries permitted a slightly greater percentage of maximum back pressure from combustion.

A simple correlation has been developed to correlate the back-pressure performance of the various inlet geometries. A plot of the normalized maximum back pressure vs the geometric contraction ratio divided by the square-root of the aspect ratio of the isolator is shown in Fig. 15. Two geometries with comparable contraction ratios may not behave in a similar manner. Consequently, the aspect ratio is used to introduce the variation of the cross-sectional shape. The solid line represents the second-order least-squares curve fit:

$$P_b/P_1 = 1.74(CR_g/\sqrt{AR})^2 - 1.73(CR_g/\sqrt{AR}) + 19.6 \tag{2}$$

While a slight dependence on ramp shape is evident, the correlation does fit the experimental data reasonably well.

Concluding Remarks

The current research focuses on the Mach 4 performance of forward-swept sidewall compression inlets with various bodyside compression surfaces. Performance characteristics such as starting behavior, mean surface pressure distributions, permissible back-pressure limits, and mass capture have been presented and discussed. Overall, the results indicate that the starting and performance characteristics of a sidewall compression inlet can be significantly modified by the presence and shape of a compression ramp located between the sidewalls. Convex ramp geometries appear much more conducive to inlet starting than concave shapes while permitting increased mass capture over comparable straight ramps. Also, the convex shape reduces the pressure loading on the cowl and permits a larger pressure difference due to combustion. Specific observations from this study are listed.

1) Five configurations started at $W/g = 3.0$ (no ramp, 4.0-, 6.2-, 8.0-deg straight ramps, and the 8.0-/5.8-/3.2-deg convex ramp). Only two configurations successfully started at $W/g = 4.0$ (the 6.2-deg straight ramp and the 8.0-/5.8-/3.2-deg convex ramp).

2) Inlet configurations using the 4.0-/8.3-deg concave ramp did not start at either value of W/g for the range of cowl positions tested.

3) Kerosene-lampblack surface tracer patterns indicated that the initial swept-forward orientation of the leading-edge shock waves had dissipated by the first sidewall impingement and the shock wave remained nearly vertical through the re-mainder of the inlet. Also seen was a large amount of flow turning along the sidewalls, especially near the cowl leading edge.

4) The $W/g = 3.0$, 8.0-deg and the $W/g = 4.0$, 6.2-deg straight-ramp configurations demonstrated the greatest permissible back pressure of just over $30P_1$.

5) The 8.0-/5.8-/3.2-deg convex-ramp configuration demonstrated increased mass capture as compared to the 6.2-deg straight ramp.

6) At both $W/g = 3.0$ and 4.0, the 8.0-/5.8-/3.2-deg convex ramp demonstrated the largest difference between maximum back pressure and throat pressure while demonstrating low throat and cowl pressures.

7) The back-pressure performance of these inlets has been correlated using geometric parameters of the inlet configuration, exclusively.

References

[1]Trexler, C. A., "Performance of an Inlet for an Integrated Scramjet Concept," *Journal of Aircraft*, Vol. 3, No. 9, 1974, pp. 589–591.
[2]Henry, J. R., and Anderson, G. Y., "Design Considerations for the Airframe-Integrated Scramjet," NASA TM X-2895, Dec. 1973.
[3]Kumar, A. J., "Numerical Simulation of Scramjet Inlet Flow Fields," NASA TP-2517, May 1986.
[4]Trexler, C. A., "Inlet Starting Predictions for Sidewall-Compression Scramjet Inlets," AIAA Paper 88-3257, July 1988.
[5]Cozart, A. B., Holland, S. D., Trexler, C. A., and Perkins, J. N., "Leading Edge Sweep Effects in Generic Three-Dimensional Sidewall Compression Scramjet Inlet," AIAA Paper 92-0674, Jan. 1992.
[6]Holland, S. D., and Perkins, J. N., "Internal Shock Interactions in Propulsion/Airframe Integrated Three-Dimensional Sidewall Compression Scramjet Inlets," AIAA Paper 92-3099, July 1992.
[7]Settles, G. S., and Dolling, D. S., "Swept Shock Wave/Boundary Layer Interactions," *Tactical Missile Aerodynamics*, edited by J. Nielsen and M. Hemsch, Vol. 104, Progress in Astronautics and Aeronautics, AIAA, New York, 1986.
[8]Settles, G. S., and Dolling, D. S., "Swept Shock/Boundary-Layer Interactions—Tutorial and Update," AIAA Paper 90-0375, Jan. 1990.
[9]Narayanswami, N., Knight, D., Bogdonoff, S. M., and Horstman, C. C., "Crossing Shock Wave-Turbulent Boundary Layer Interactions," AIAA Paper 91-0649, Jan. 1991.
[10]Garrison, T. J., Settles, G. S., Narayanswami, N., and Knight, D. D., "Structure of Crossing-Shock Wave/Turbulent Boundary-Layer Interactions," AIAA Paper 92-3670, July 1992.
[11]Bogdonoff, S. M., and Stokes, W. L., "Crossing Shock Wave Turbulent Boundary Layer Interactions—Variable Angle and Shock Generator Length Geometry Effects at Mach 3," AIAA Paper 92-0636, Jan. 1992.
[12]Hudgens, J. A., and Trexler, C. A., "Operating Characteristics at Mach 4 of an Inlet Having Forward-Swept, Sidewall-Compression Surfaces," AIAA Paper 92-3101, July 1992.
[13]Wilcox, D. C., "Program EDDYBL User's Guide," DCW Industries Rept. DCW-R-NC-04, 1987.
[14]McClinton, C. R., "The Effect of Injection Angle on the Interactions Between Sonic Secondary Jets and a Supersonic Free Stream," NASA TN D-6669, Feb. 1972.
[15]Settles, G. S., and Teng, H.-Y., "Flow Visualization Methods for Separated Three-Dimensional Shock Wave/Turbulent Boundary Layer Interactions," *AIAA Journal*, Vol. 21, No. 3, 1983, pp. 390–397.
[16]Kline, S. J., and McClintock, F. A., "Describing Uncertainties in Single-Sample Experiments," *Mechanical Engineering*, Vol. 75, Jan. 1953, pp. 3–8.